

Microstructure and properties of FeCoCrNiMoSi_x high-entropy alloys fabricated by spark plasma sintering

Yucheng Yang ^a, Yaojia Ren ^a, Yanwen Tian ^a, Kaiyang Li ^b, Weidong Zhang ^c,

Quan Shan ^{d,***}, Yingtao Tian ^e, Qianli Huang ^{a,**}, Hong Wu ^{a,*}

^a *State Key Laboratory of Powder Metallurgy, Central South University, Changsha 410083, P.R. China;*

^b *Department of Chemical and Materials Engineering, University of Alberta, Edmonton, Alberta, T6G 1H9, Canada;*

^c *College of Materials Science and Engineering, Hunan University, Changsha 410082, P.R. China;*

^d *Academy of Materials Science and Engineering, Kunming University of Science and Technology, Kunming, P.R. China;*

^e *Department of Engineering, Lancaster University, Bailrigg, Lancaster LA1 4YW, United Kingdom.*

** Corresponding author.*

*** Corresponding author.*

**** Corresponding author.*

E-mail address:

hwucsu@csu.edu.cn; wuhong927@126.com (Hong Wu),

hql1990@163.com (Qianli Huang),

quanshan.ms@gmail.com (Quan Shan).

Abstract

FeCoCrNiMoSi_x ($x = 0.5, 1.0, 1.5$) high-entropy alloys (HEAs) were successfully fabricated by spark plasma sintering (SPS). The microstructure, tribological properties, oxidation behaviors and corrosion resistance of the HEAs were systematically investigated. The experimental results showed that the microstructure mainly consisted of Fe-rich face-centered-cubic (FCC) phase, Mo-rich FCC phase solid solution and various of Si-rich intermetallics, where the elevated Si content coarsened the primary Mo-rich phase into dendritic eventually. These Mo-rich dendrites possessed strong covalent-dominant atomic bonds that enhanced the microhardness (from 725 to 1186 HV) and wear resistance. The FeCoCrNiMoSi_{0.5} HEA exhibited an outstanding combination of relatively high wear resistance, the strongest oxidation resistance under 800 °C at among the three alloy compositions. The corrosion resistance of HEAs showed an increasing trend with the elevated Si content, and FeCoCrNiMoSi_{1.5} presented the best performance.

Keywords:

FeCoCrNi, high-entropy alloy, Si, tribological behavior, corrosion resistance, spark plasma sintering

1. Introduction

High entropy alloys (HEAs) are a new family of alloys commonly consisting of 5 or more principal alloying elements [1-3]. Comparing with traditional alloys which usually have single principal element, HEAs tend to form disordered solid solutions rather than intermetallic compounds owing to their high mixing entropy [4, 5]. The nearly same proportion of all metal elements leads to significant disordering of the structure in the liquid status [6, 7]. Each element in the HEA system can be seen as a solute atom because there is no dominating matrix element in HEAs. This contributes to the uniform distribution of various elements in alloy structure [8]. In addition to the increased entropy, a large number of phases can also be obtained through altering the alloy combinations, leading to enormous possibilities and magnificent potentials in achieving superior material properties and performances.

Over the past few decades, HEAs have been widely studied due to the combination of exceptional properties, such as prominent mechanical properties, low thermal conductivity and excellent catalytic activity, which can not be obtained in conventional materials [9-11]. FeCoCrNi HEA, which presents good corrosion resistance, could be equipped with further enhanced mechanical properties through phase-controlling methods. In the study carried out by Tang et al. [12], nano-twinning has been observed due to the existence of two-phase FCC in $Al_{0.5}CoCrCuFeNi$ HEA, which resulted in a high tensile strength. Also, high strengths (916-1517 MPa) were obtained by Li and Liang et al. [13, 14] with the addition of Mo in FeCoCrNiMn HEA due to the increased

amount of amorphous phase using selective laser melting. A face-centered-cubic (FCC)/body-centered-cubic (BCC) dual-phase structure was reported in $\text{Fe}_x\text{CoCrNiMn}$, which achieves both high strength and elongation rate (600 MPa and 67%) with 67 at.% Fe [15]. A 786 MPa ultimate tensile strength and over 50% elongation $\text{FeCoCrNiMo}_{0.23}$ HEA was fabricated by powder metallurgy featuring a single FCC structure resulted from Mo addition [16, 17]. In addition to mechanical properties, the corrosion resistance could also be improved by controlling the alloying elements. For example, Mo can enhance the corrosion resistance of FeCoCrNi HEA by changing the microstructure [4]. A unique structure consisted of Cr-Fe rich equiaxed grains with Al-Ni rich grain boundaries and Al-rich particles in homogenized $\text{Al}_{0.5}\text{CoCrFeNi}$ HEA can also improve the corrosion resistance [18]. Additionally, wear behavior and hardness of FeCoCrNi HEA system have been studied in depth by researchers to widen the applications. FeCoNiCuAl HEAs with high hardness (about 8.4 GPa) and good topological behaviors were successfully fabricated using laser powder bed fusion [19]. As reported by Liu et al. [20], FeCoCrNi HEA acquired adjustable hardness increase achieved with the addition of WC. $\text{Al}_{35}\text{Cr}_{14}\text{Mg}_6\text{Ti}_{35}\text{V}_{10}$ HEA possessed one hexagonal close-packed (HCP) phase and two BCC phases microstructure was fabricated using SPS with minor contamination of WC and acquired a hardness of 460 HV, which is superior to light-weight conventional alloy [21, 22]. In another study carried out by Fourmont et al. [23], a hard (670 HV) and dense AlCoCrFeNi HEA was synthesized by SPS owing to the formation of a nano-lamellar microstructure with the coexistence of the FCC and BCC phases. According to Yurkova et al [24], three-phase AlCuNiFeCr

HEA consisting mainly of one B2-ordered solid solution, one FCC and the $(\text{Cr, Fe})_{12}\text{C}_6$ phase, was produced after annealing and SPS, which manifested ultra-high hardness of 8.35 GPa.

Silicon, as the second most abundant element in the Earth crust and a strengthening component to improve alloy properties, has a great potential to replace many high-cost alloying elements in FeCoCrNi HEA system [25]. The microstructure can be optimized through various Si content, which leads to different properties and functions. The high melt point of Si also provides good anti-oxidation ability at elevated temperatures [26]. According to Tsai et al. [27], a Cu/HEA(AlMoNbSiTaTiVZr)/Si sandwich structure was designed to prevent inter-diffusion of Cu and Si, which presented high mechanical properties. As declared by Kumar et al. [28], the increase of Si from 0 to 0.9 wt% promoted the formation of BCC phase to a dominant extent, compared with the amount of FCC phase. According to Babilas et al. [29], Si gives a negative enthalpy owing to the precipitation of an intermetallic Cr_3Si phase and segregation of iron in AlCoCrFeNi. The addition of Si can also improve the oxidation resistance in the NbCrMoTiVAl_{0.5}Si_{0.3} and equal atomic NbMoCrTiAl systems [30]. Moreover, it has been proved that the addition of Si resulted in the formation of the MoSi-rich phase in AlCoCrNiMoFeSi claddings, which offered an improvement of tribological behaviors [31]. Therefore, it has been demonstrated that Si could be a potential strengthening element to improve the properties and performance of a number of HEAs. It is still of great significance to investigate the fundamentals of how Si affects the microstructure evolution and mechanical properties of HEAs and explore further possibilities of

adding Si into the new alloys for achieving exceptional properties and performances.

Spark plasma sintering (SPS) has been widely employed in materials process research for its characteristics of making the samples denser [32]. In this study, silicon was added to FeCoCrNiMo HEA system aiming to improve the corrosion and tribological behaviors in a cost-effective fashion. FeCoCrNiMoSi_x (x=0.5, 1.0, 1.5) HEAs were fabricated by SPS to obtain fully dense samples. Microstructure, hardness, tribological property and corrosion resistance (including both high temperature oxidation and aqueous corrosion) were systematically investigated. Prominent corrosion resistance, hardness, tribological behavior and stable anti-oxidation ability in high temperature were obtained with the addition content of Si.

2. Materials and Methods

2.1 Alloy production

The experimental materials were prepared using the mixture of pure Fe, Co, Cr, Ni, Mo and Si with the atomic ratio of 1: 1: 1: 1: 1: x. Here x is 0.5 (FeCoCrNiMoSi_{0.5}, i.e. Fe_{18.18}Co_{18.18}Cr_{18.18}Ni_{18.18}Mo_{18.18}Si_{9.1}), 1 (FeCoCrNiMoSi_{1.0}, i.e. Fe_{16.67}Co_{16.67}Cr_{16.67}Ni_{16.67}Mo_{16.67}Si_{16.67}) and 1.5 (FeCoCrNiMoSi_{1.5}, i.e. Fe_{15.38}Co_{15.38}Cr_{15.38}Ni_{15.38}Mo_{15.38}Si_{23.1}). Gas atomization was used to ensure that the particle size of mixed powder is uniform. The specific mass percentage is shown in Table 1. FeCoCrNiMoSi_{0.5} HEA atomized powders were sintered using SPS under 1150 °C with a heating rate of 100 °C/min.

Table 1. The specific mass percentages (wt%) of elements in powders

	Fe	Co	Cr	Ni	Mo	Si
FeCoCrNiMoSi _{0.5}	16.20	17.30	15.50	18.00	28.40	4.50
FeCoCrNiMoSi _{1.0}	15.60	16.50	14.80	17.10	27.40	8.50
FeCoCrNiMoSi _{1.5}	15.30	15.60	14.70	16.80	25.10	11.80

2.2 Phase composition

X-ray diffractometer (XRD) was performed to examine the phases constitution of the specimens. The data were collected by a PIGAKV D/Max 2550 X-ray diffractometer with Cu K α ray radiation operated at 40 kV and 200 mA. Measurements were performed by step scanning 2 θ from 30 ° to 90 ° with a step of 0.02 %.

2.3 Microstructural characterization

The surface of each sample was polished with 80 #, 320 #, 600 #, 100 #, 1500 # and 2000 # grit sand paper respectively followed by a 1 μ m diamond paste polishing and a 0.04 μ m alumina suspension finishing. A Quanta 250 FEG (FEI company) scanning electron microscopy (SEM) was used to observe the morphology and microstructure of the block specimens.

2.4 Microhardness and tribological behavior

The Vicker microhardness of the HEAs were measured using a HVS-5 digital

Vickers hardness tester at a load of 30 N. A HT-1000 pin disk high temperature friction and wear testing machine (Lanzhou KaiHua Central technology) was utilized to measure the friction and wear performance of SPS HEAs using Si₃N₄ ceramic ball as the grinding material with a load of 20 N. The relative friction velocity and distance are 0.5 m/s and 1050 m, respectively. Grinding scratch and adhesive debris were observed using SEM.

2.5 High temperature stability

TG-DSC experiment was performed on a Q2000 differential scanning calorimeter (DSC) conducted by Stream Company. The protective atmosphere was nitrogen and the heating rate was 30 °C/min. The high temperature antioxidant experiment adopted the cyclic high temperature oxidation method. Samples and experimental crucible were put into the annealing furnace at 800 °C for 10 h of high temperature oxidation. Then the specimens were air-cooled to room temperature and their mass was measured. The specimens were put into the furnace again for high temperature oxidation for 10 h, and the above steps were repeated. This cycle was repeated ten times for a total oxidation of 100 h. The morphology of oxidation film was observed using SEM.

2.6 Electrochemical characterization

Electrochemical corrosion test was conducted in 1 mol/L of sulfuric acid. Anodic polarization curves were measured using a CHI660E electrochemical workstation (employing a saturated calomel electrode (SCE) and a platinum electrode as the

reference electrode and auxiliary electrode, respectively). The voltage was sweeping from -0.5 V to 0.1 V at a 0.005 V/s scanning speed. The morphologies of the resultant corroded surfaces were examined using SEM.

3. Results and discussion

3.1 Phase composition

The phase compositions are shown in Fig. 1. The FeCoCrNiMoSi_x (x = 0.5, 1.0, 1.5) HEAs fabricated by SPS were mainly composed of Fe-rich FCC phase and Mo-rich FCC phase. Moreover, the diffraction peaks show that the intensities of Mo-rich FCC phase peaks improve significantly with the Si ratio changing from 1.0 to 1.5 atomic ratio.

In order to better explain the effect of Si element, three equations are employed as follows. Through the calculation of equation (1)

$$\varepsilon = |\Delta\alpha / \alpha_0| \quad (1),$$

where $\Delta\alpha = |\alpha - \alpha_0|$, α_0 and α is the lattice constant of actual alloy crystal and theoretical crystal, respectively [33]. The high ε value of HEAs indicates an inferior tendency of FCC phase formation with increasing Si content. This demonstrates an enhancement of solid solution strengthening effect with the addition of silicon content [34]. Moreover, valence electron concentration (VEC) is calculated through equation (2),

$$VEC = \sum_{i=1}^n c_i(VEC)_i \quad (2)$$

where $(\text{VEC})_i$ is VEC for the individual element [35]. Here in, the parameter δ is also used to describe the i_{th} comprehensive effect of the atomic-size difference in each element alloy [36], which can be expressed as the following equation:

$$\delta = 100 \sqrt{\sum_{i=1}^n c_i \left(1 - \frac{r_i}{\bar{r}}\right)^2} \quad (3)$$

$$\bar{r} = \sum_{i=1}^n c_i r_i \quad (4)$$

where c_i is the atomic percentage of the i_{th} component, \bar{r} presents the average atomic radius and r_i is atomic radius [37]. Through calculation, the VEC decreases and δ increases with the increasing silicon content. This compresses the formation of FCC phase [20]. It can be concluded that Si addition is beneficial to the formation of two FCC phases.

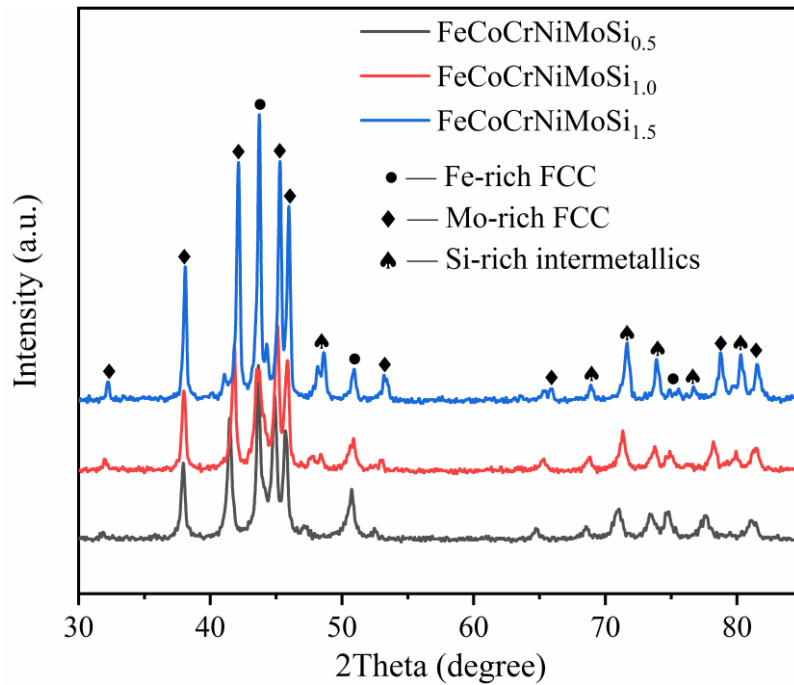


Fig. 1. XRD analysis of SPS HEAs bulk samples

3.2 Microstructure analysis

The microstructure of SPS FeCoCrNiMoSi_x (x = 0.5, 1.0, 1.5) HEAs are shown in Fig. 2. It is clear that the dark phase of FeCoCrNiMoSi_x (x = 0.5, 1.0) SPS HEAs was annular with similar dimensions with the disordered and evenly spaced distribution. In contrast, the white phase of FeCoCrNiMoSi_{1.5} HEAs was observed to be dendritic. According to EDS analysis, the white phase was mainly composed of Mo-rich FCC phase while the dark phase consisting of Fe-rich FCC phase, which has a similar result with Chen et al [31]. Figure 3 presents the area percentage of Fe-rich and Mo-rich phases in Fig. 2. Continuous increment of Mo-rich phase area fraction was found with increasing silicon content, which shares the same conclusion with XRD analysis.

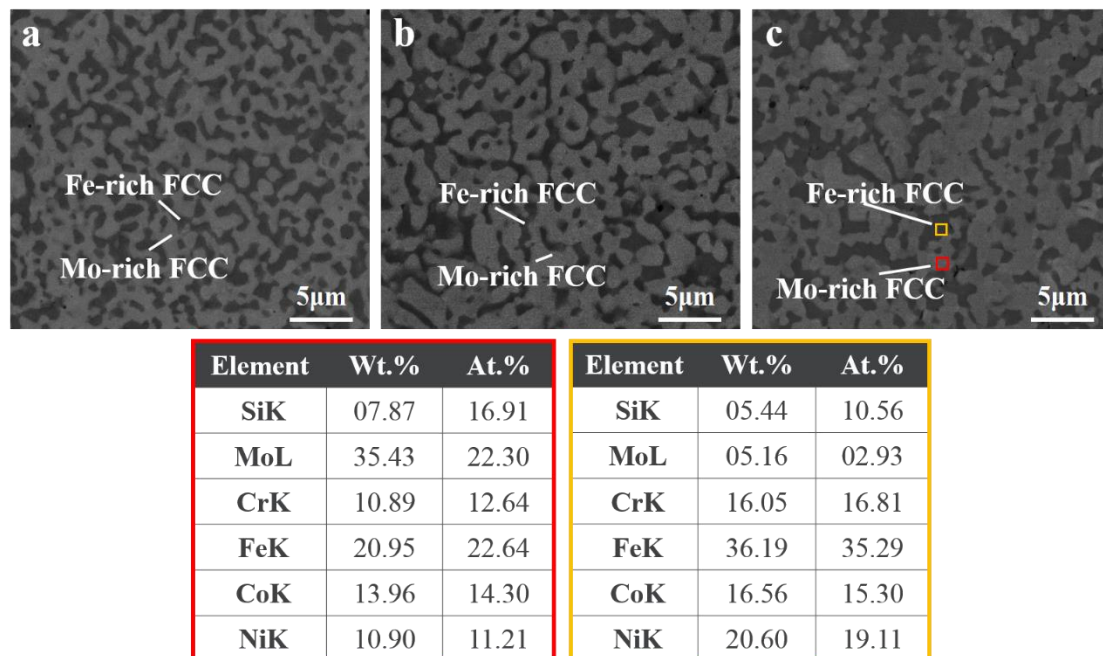


Fig. 2. The microstructure morphology and EDS analysis (red and orange box in c) of SPS HEAs.

(a) FeCoCrNiMoSi_{0.5}, (b) FeCoCrNiMoSi_{1.0}, (c) FeCoCrNiMoSi_{1.5}

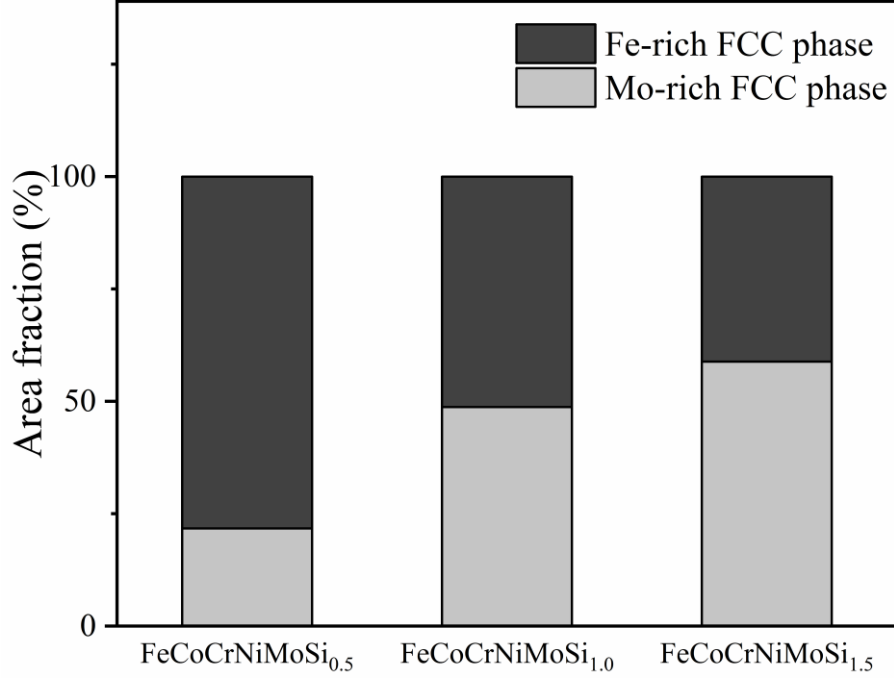


Fig. 3. The volume fraction of Fe-rich and Mo-rich phases.

3.3 Microhardness and tribological behaviors

Figure 4 presents the hardness and wear rate in tribological tests of the HEAs prepared by SPS. Wear rate was calculated using the equation [38]:

$$R = V_{loss}/N S \quad (5)$$

where R presents the wear rate ($\text{mm}^3 \text{N}^{-1} \text{m}^{-1}$), V_{loss} (mm^3) presents the volumetric loss and obtains from M_{loss}/ρ (where M_{loss} is the mass loss after wear test and ρ presents the density of three samples), N (N) is the applied load and S (m) is the total sliding distance. Specific values compared with others HEA were listed in Table 2. The hardness of the HEAs increased obviously from 725 HV to 1186 HV with the reduction of the Fe-rich phase which was induced by the increase of Si content. This can be attributed to the appearance of strong interaction between silicon and other elements in the Mo-rich

phase dendritic region [39]. The radius of Si atom is smaller than other alloying elements, resulting in lattice distortion certain solid solution strengthening [40]. Also, the Si-rich hard intermetallics, has a complex hexagonal crystalline structure known for the characteristic of high hardness. The wear rate presents a reduction tendency with the addition of Si content. FeCoCrNiMoSi_{0.5} presents the best wear resistance because of the lower wear rate. It should be noted that wear rate shown in Fig. 4 has an abnormal increase compared with the enhancement of hardness.

Table 2. A comparison on microhardness and wear rate of several FeCoCrNi-based HEAs.

Material	Process	Microhardness (HV)	Wear rate ($\times 10^{-4}$ mm ³ N ⁻¹ m ⁻¹)
FeCoCrNi [41]	As-cast	150	\
FeCoCrNi [42]	As-annealed	200	\
FeCoCrNiMo _{0.3} [41]	As-cast	200	\
FeCoCrNiMo _{0.3} [42]	As-annealed	270	\
FeCoCrNiMo _{0.3} [43]	As-SPS	450	3.250
FeCoCrNi(WC) _{0.1} [44]	As-plasma cladding	300	0.303
FeCoCrNiMoSi _{0.5} (this work)	As-SPS	725	0.292
FeCoCrNiMoSi _{1.0} (this work)	As-SPS	790	0.764
FeCoCrNiMoSi _{1.5} (this work)	As-SPS	1186	0.892

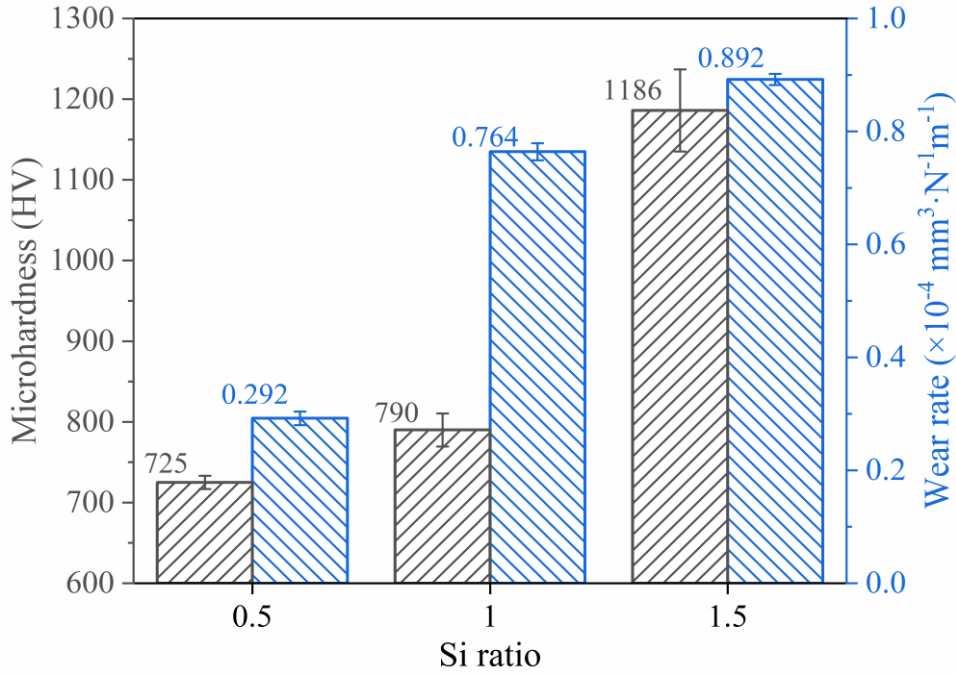


Fig. 4. The hardness and wear rate in friction and wear process of the SPS HEAs

The coefficient of friction (COF) of the SPS HEAs are shown in Fig. 5. The average values of the COF are 0.369, 0.415 and 0.403, respectively.

To clearly explain the results of Fig. 4 and 5, further exploration needs to be investigated. Figure 6 presents the results of the debris size and EDS analysis. Figures 7(a)-(c) are the morphologies of the worn surface of SPS HEAs. The total area and average debris size of three samples were calculated by Image J (Table 3). The debris of $\text{FeCoCrNiMoSi}_{1.0}$ and $\text{FeCoCrNiMoSi}_{1.5}$ HEAs has a higher concentration of oxygen. In contrast, debris of $\text{FeCoCrNiMoSi}_{0.5}$ presents a much small size. As shown in Fig. 6, Fig. 7 and Table 3, the size of wear debris is small and many scratches appear in the wear interface in $\text{FeCoCrNiMoSi}_{0.5}$. Moreover, the outer ring of the worn surface in $\text{FeCoCrNiMoSi}_{0.5}$ HEAs was squeezed by the friction pair, revealing typical characteristics of abrasive and adhesive wear [45, 46]. The combination of grooves

(shown in Fig. 7 (a)) and the much smaller size of debris (shown in Fig. 6), indicates that the abrasive wear predominates during the wear process [47, 48]. A major proportion of abrasive and adhesive wear results in a relatively low wear rate. On the contrary, many peeling-off of larger sized wear debris are shown in Fig. 6 (b) and (c) and these two component samples were mainly peeled and abraded (shown in Fig. 7) during the wear process, which demonstrates a typical delamination wear [49]. High proportion of delamination wear induces a larger value of wear rate in $\text{FeCoCrNiMoSi}_{1.0}$ and $\text{FeCoCrNiMoSi}_{1.5}$ [50]. In a word, the value of wear rate and COF of FeCoCrNiMoSi_x HEAs was determined by the wear mechanism. The wear resistance of $\text{FeCoCrNiMoSi}_{1.0}$ and $\text{FeCoCrNiMoSi}_{1.5}$ HEAs are significantly reduced compared with that of $\text{FeCoCrNiMoSi}_{0.5}$. This is because the proportion of delamination wear and adhesive wear gradually increases with the addition of Si, which leads to more wear rate.

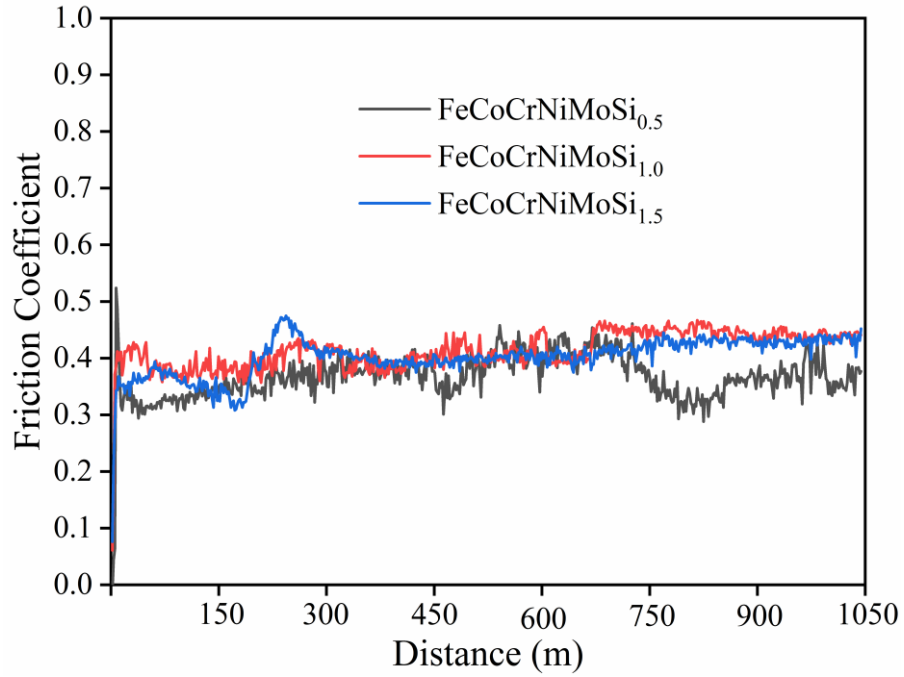


Fig. 5. The COF of the SPS HEAs

Table 3. The analysis of debris size calculated by Image J

	Total area (μm^2)	Percentage of large size ($> 25 \mu\text{m}^2$) debris(%)
FeCoCrNiMoSi _{0.5}	558.20	0.06
FeCoCrNiMoSi _{1.0}	680.17	18.00
FeCoCrNiMoSi _{1.5}	1015.92	41.86

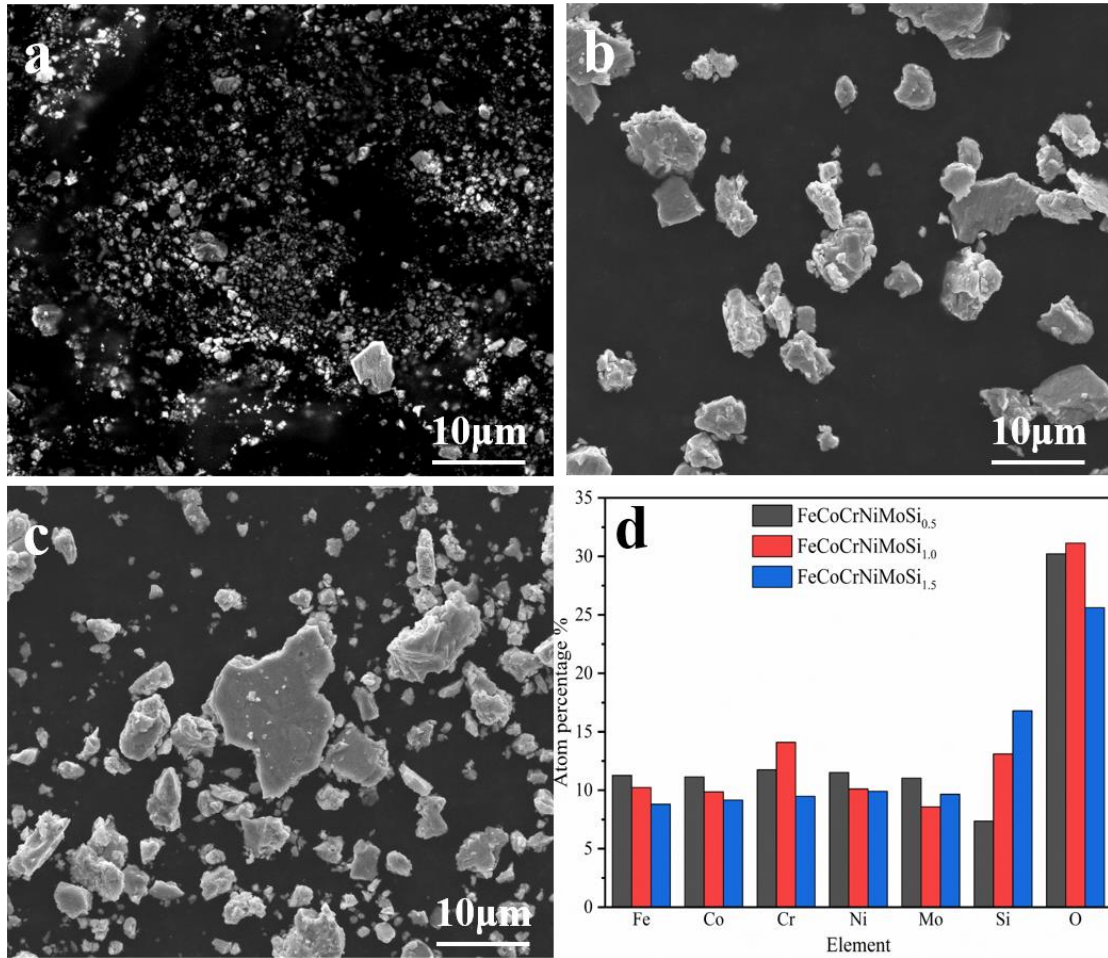


Fig. 6. The morphology of wear debris produced during friction and wear of the three HEAs:
 (a) FeCoCrNiMoSi_{0.5}, (b) FeCoCrNiMoSi_{1.0}, (c) FeCoCrNiMoSi_{1.5}; (d) the EDS analyses of the debris

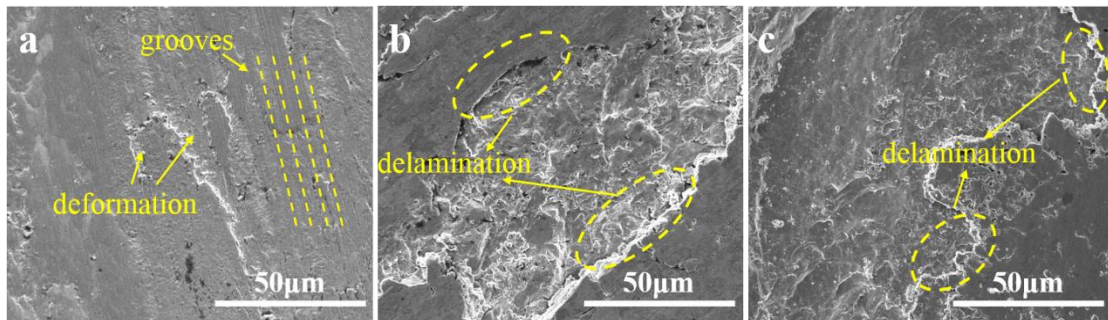


Fig. 7. The morphology of the wear interface of the SPS HEAs
 (a) FeCoCrNiMoSi_{0.5}, (b) FeCoCrNiMoSi_{1.0}, (c) FeCoCrNiMoSi_{1.5}

3.4 High temperature oxidation property

As shown in Fig. 8, during the heating process from room temperature to 1150 °C, the TG curves of the three HEA samples are relatively stable and no significant thermal effect peak could be observed. No phase changes happened in this temperature range, showing a relatively strong high-temperature stability of FeCoCrNiMoSi_x HEAs.

The weight gain of FeCoCrNiMoSi_x was tested every ten hours as a function of the exposure time at 800 °C, over a period of 100 h. Before the as-sintered FeCoCrNiMoSi_x HEAs were oxidized for the high-temperature cyclic test at 800 °C, the crucible used in the experiment was annealed at high temperature to make its quality stable. Data about weight gain obtained from oxidation tests were expressed in equation (6):

$$\Delta G = (m_x - m_0) / S_0 \quad (6),$$

where m_x presents the final mass of HEAs, m_0 presents the original mass of HEAs and S_0 presents the total area exposed for oxidation. However, because the value of ΔG was very small, the weight gain will be squared so that the change in mass can be observed more intuitively. It is evident in Fig. 9 (d) that the quality of the three samples presents no obvious fluctuation during the heating process under 50 hours, showing a relatively high resistance to high temperature oxidation below 800 °C. Besides, FeCoCrNiMoSi_{1.5} presents a larger value of weight gain comparing to that of FeCoCrNiMoSi_{0.5} and FeCoCrNiMoSi_{1.0}. The parabolic rate constant (k_p) thus can be calculated by the following equation:

$$\left(\frac{\Delta m}{A}\right)^2 = k_p t \quad (7)$$

where Δm , A , k_p and t present mass change, surface area of samples, parabolic rate constant and oxidation time, respectively. Values compared with others research about k_p were shown in Table 4. Obviously, the FeCoCrNiMoSi_{0.5} HEA presents a dominant oxidation resistance compared with that of FeCoCrNiMn systems.

Figure 9 (a)-(c) demonstrate the surface morphology of the oxidation tests of FeCoCrNiMoSi_x HEAs after high temperature oxidation. The formation of oxide particles on the surface is the most significant characteristic of the FeCoCrNiMoSi_x HEAs. With increasing Si content, the surface oxides exhibits a growing trend with the average particle size increased from several hundred nanometers to several micrometers. It indicates the growth of surface oxides and enhanced oxidation, which is in consistent with the weight gain trend in Fig. 9(d). Also, the high temperature oxidation film on FeCoCrNiMoSi_{1.5} is much thicker than that of FeCoCrNiMoSi_{0.5} and FeCoCrNiMoSi_{1.0}. In this case, the high Cr contents and a sluggish diffusion effect might be responsible for the significant oxidation resistance properties [51]. Moreover, oxidation tends to form at initial defects like cracks, which occurred abundantly in FeCoCrNiMoSi_{1.5} during the solidification process [52]. Si has the highest oxytropy in FeCoCrNiMoSi HEA system [53]. While an appropriate amount of Si could help to form an interlayer between the outer oxide and the metal as a diffusion barrier, excess Si will lead to the opposite effect [54]. As shown in previous XRD analysis (Figure 1), increasing Si content enhances the formation of Si-rich intermetallic. It is postulated that too much

intermetallic in FeCoCrNiMoSi_{1.5} may hinder the formation of a continuous surface chromium oxide layer or provide extra diffusion paths for the outward diffusion of metallic ions and the inward ingress of oxygen, leading to enhanced oxidation. A previous study also found that in Ta-Mo-Cr-Ti-Al HEA system, the addition of Si slightly deteriorates the oxidation resistance due to the enhanced formation of laves phase and the resulting internal oxidation [55].

Table 4. The k_p values among several FeCoCrNi system HEAs.

Material	Parabolic rate constant k_p (mg ² cm ⁻⁴ h ⁻¹) at 800 °C
FeCoCrNiMoSi _{0.5} (this work)	0.0002
FeCoCrNiMoSi _{1.0} (this work)	0.0004
FeCoCrNiMoSi _{1.5} (this work)	0.0021
FeCoCrNiMn [56]	0.0997
FeCoNiCrMn [57]	0.0600
FeCoNiCrMn [58]	0.0540
CoFeCrMnNi [59]	0.0432

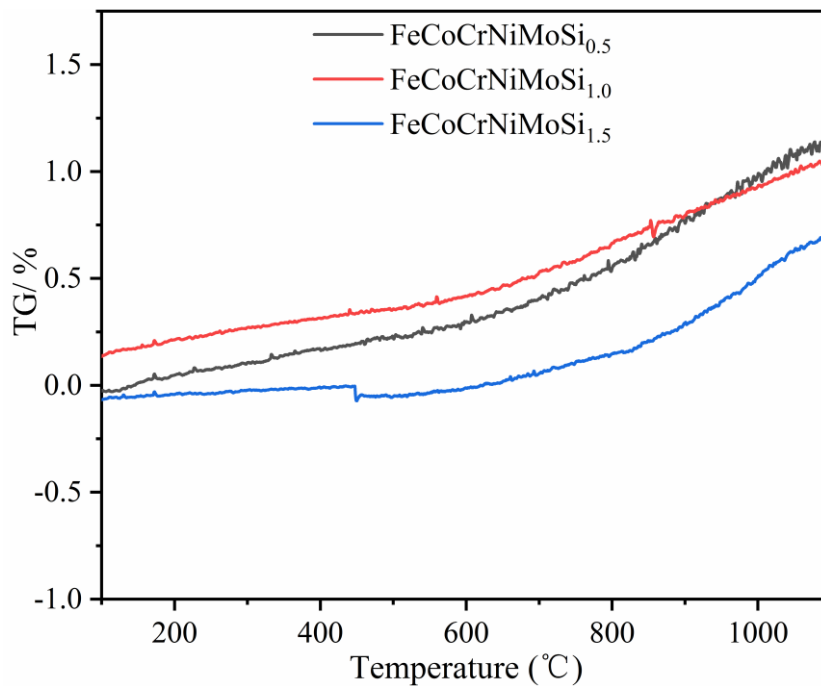


Fig. 8. The TG curves of the HEAs prepared by SPS

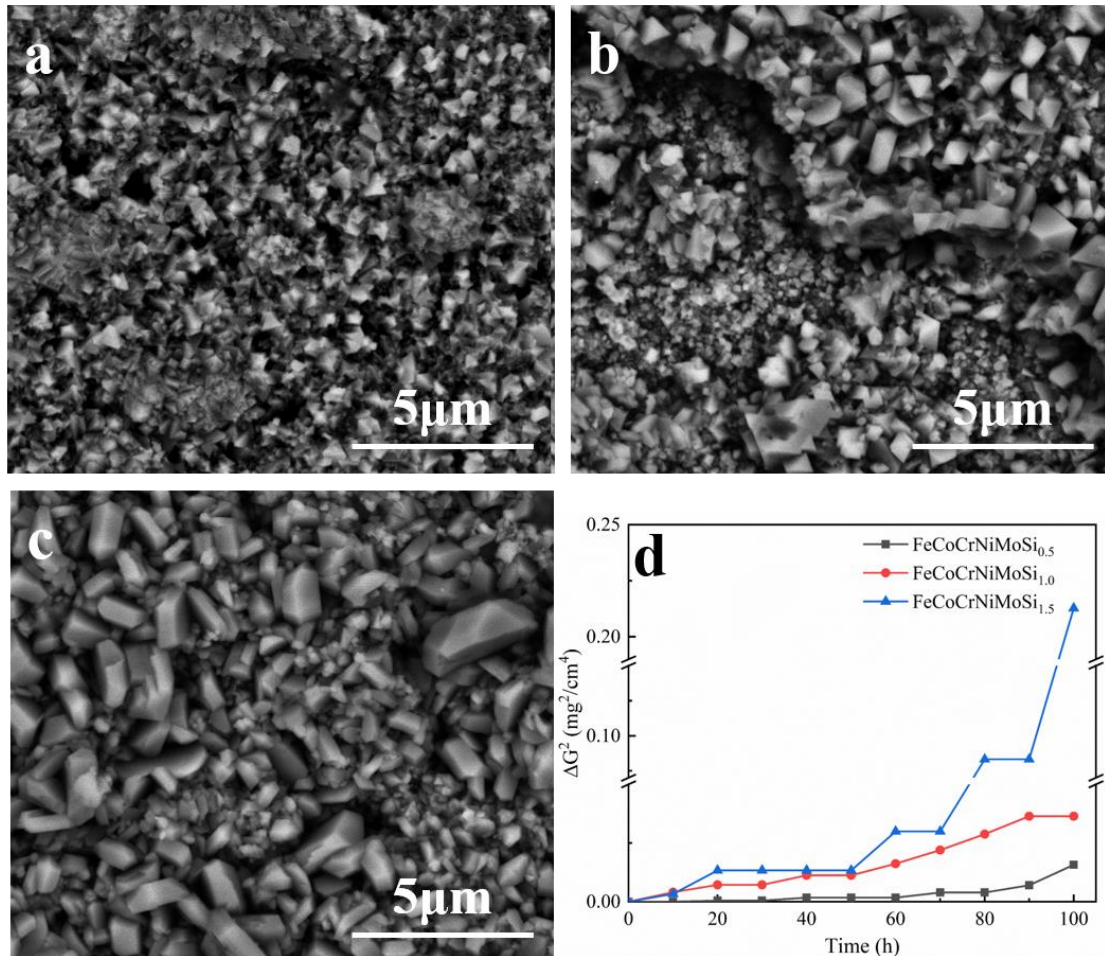


Fig. 9. The surface morphology of the HEAs after high temperature oxidation. (a) FeCoCrNiMoSi_{0.5}, (b) FeCoCrNiMoSi_{1.0}, (c) FeCoCrNiMoSi_{1.5}; (d) the oxidation kinetic curves of the three HEAs for 100 h at 800 °C.

3.5 Corrosion resistance

Both immersion and electrochemical tests were conducted to evaluate the corrosion resistance of HEAs. During the immersion tests, HEAs were immersed in 1 mol/L H₂SO₄ solution at room temperature for 30 days and the microscopic morphologies of three kinds of HEAs after immersion tests are shown in Fig. 10.

From Fig. 10 (a)-(c), the corrosion pits can be seen on the surface and tend to be smaller and shallower with increasing Si content. The related corrosion parameters are shown in Table 5. Note that the corrosion rate was calculated through the following equation [60]:

$$CR_{im} = (K \times W) / (A \times T \times D) \quad (8)$$

where CR_{im} is the immersion corrosion rate (mm/y), K is a constant, which is 8.76×10^4 , A is the exposed area (cm^2), T is the time of exposure (h), W is the mass loss (g) and D is the density (g/cm^3). Moreover, Table 5 presents no significant mass change after the corrosion. The reduced mass change ratio and corrosion rate with increasing Si show a consistent tendency with the SEM morphology observations. The CR_{im} of this HEA (1.31×10^{-2} mm/y) is much lower than that of 304L alloys (1.9039 mm/y) [61], representing a relatively high corrosion resistance of HEAs and their potential application in engineering field. Through the corrosion rate in Table 5 and the morphology of corrosion surface in Fig. 10, it is obvious that the corrosion resistance of the alloy is enhanced with the increasing atomic Si content owing to the high corrosion potential of Si [62]. In summary, FeCoCrNiMoSi_{1.5} HEA showed the strongest corrosion resistance immersed in 1 mol/L H₂SO₄ solution for 31 days, while the other two HEAs were similar in corrosion resistance, both inferior to FeCoCrNiMoSi_{1.5} HEA. This is in accordance with the results reported by Babilas et al. [29].

Table 5. Results of the HEAs before and after immersion in 1 mol/L H₂SO₄ solution

	FeCoCrNiMoSi _{0.5}	FeCoCrNiMoSi _{1.0}	FeCoCrNiMoSi _{1.5}
Mass change ratio (mg/cm ²)	0.9273	0.6737	0.4446
CR_{im} (mm/y)	1.31×10^{-2}	9.95×10^{-3}	6.78×10^{-3}

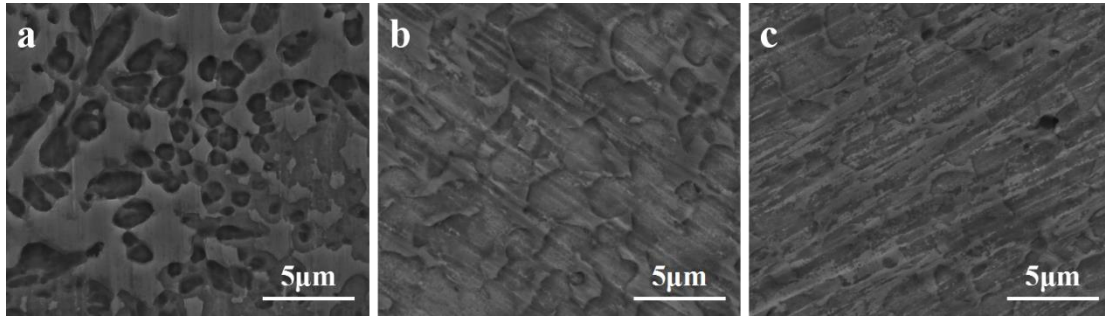


Fig. 10. The corrosion surface morphology of the SPS HEAs immersed in 1 mol/L H₂SO₄ solution for 31 days, respectively.

(a) FeCoCrNiMoSi_{0.5}, (b) FeCoCrNiMoSi_{1.0}, (c) FeCoCrNiMoSi_{1.5}

The polarization curves of HEAs in 1 mol/L H₂SO₄ solution are shown in Fig. 11.

Corrosion current density was calculated through equation (9) [63]:

$$i_{cor} = \frac{I_{cor}}{A} \quad (9)$$

where i_{cor} is corrosion current density ($\mu\text{A}/\text{cm}^2$), I_{cor} is the total anodic current (μA) and A is the exposed specimen area (cm^2). With the help of corrosion current density, the corrosion rate could be calculated as metal consumption rate in mm per year through the following equation [64, 65]:

$$CR_{cor} = K \frac{i_{cor}}{\rho} EW \quad (10)$$

where CR_{cor} represents the penetration rate (mm/yr), K is a constant (3.27×10^{-3}), ρ represents the alloy density (g/cm^3) and EW represents the alloy equivalent weight calculated in following equation [63]:

$$EW = \frac{1}{\sum \frac{n_i f_i}{W_i}} \quad (11)$$

where f_i represents the mass fraction of the i^{th} element in the HEAs, W_i is the atomic weight of the i^{th} element in HEAs and n_i is the valence of the i^{th} element of HEAs. The detailed values above are presented in Table 6. According to Table 6, the i_{cor} and CR_{cor} value of FeCoCrNiMoSi_{1.5} are the lowest, which demonstrates a better corrosion resistance. The calculated E_{cor} and i_{cor} are lower than that of the Fe-17.5Cr alloys, Fe-18Ni and mild steel, whose E_{cor} s and i_{cor} s are -0.5, -0.8 and -0.518 V and 112, 6.3 and 176 $\mu\text{A}/\text{cm}^2$, respectively [66-68]. In addition, CR_{cor} of this three HEAs are also presented low value compared with that of other alloys, such as pure aluminum alloy (CR_{cor} of 2.07 mm/yr) [69]. Adding Si content not only leads to an enhancement in the formation of intermetallics [70], but also reduces the amount of metal cation, both leading to a lower self-etching current density. It seems that the former is more detrimental during high temperature oxidation, while the latter plays a dominant role in aqueous corrosion. Note that the values of CR_{im} are lower than that of CR_{cor} as a result of the oxidation of metals induced by applied current, which can not occur in 1 mol/L H₂SO₄ because of the relatively weak oxidability. Presented in Fig. 11, the passivation regions of the two lower Si content HEAs were large owing to the formation of dense Cr₂O₃ film [71]. Additionally, a moderate Mo content in HEAs could also promote the transformation from hydroxides to oxides as a passive film and enhance the proportion of Cr₂O₃ film [72]. However, the polarization curve of FeCoCrNiMoSi_{1.5} HEA presents a narrow passivation range. The FeCoCrNiMoSi_{1.5} exhibits the narrowest passive region mainly attributed to the large amount of intermetallic particles as galvanic couples. The abundant intermetallic particles such as FeMoSi and Co₃Si can damage

the compositional uniformity and the covering integrity of the passive film, inducing a weaker corrosion passivation [72-75].

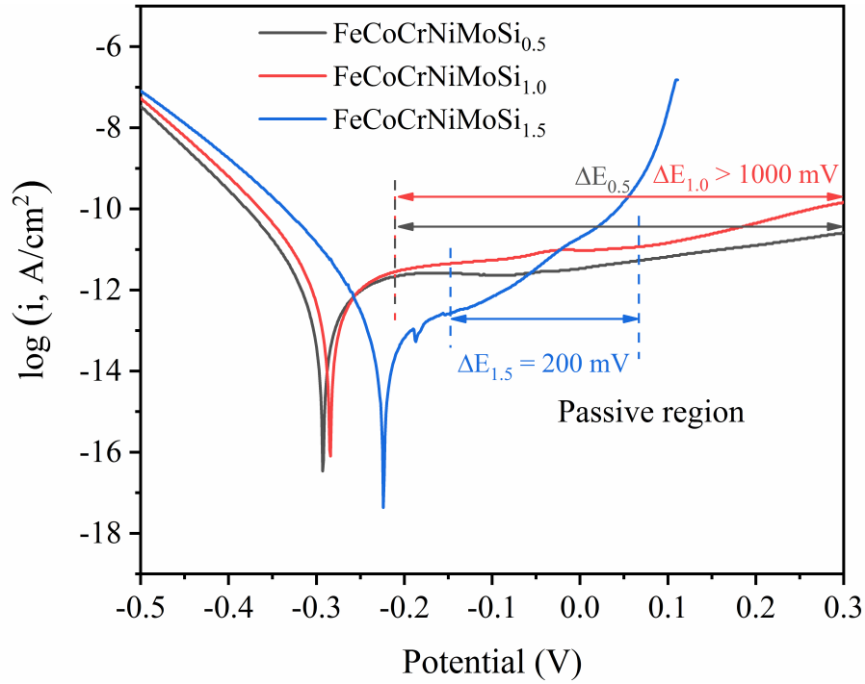


Fig. 11. The polarization curves of HEAs in 1 mol/L H₂SO₄ solution

Table 6. Specific corrosion values of HEAs in 1 mol/L H₂SO₄ solution derived from electrochemical tests

	FeCoCrNiMoSi _{0.5}	FeCoCrNiMoSi _{1.0}	FeCoCrNiMoSi _{1.5}
ρ (g/cm ³)	8.36	7.98	7.72
E_{cor} (V)	-0.293	-0.284	-0.224
i_{cor} (μ A/cm ²)	38.15	32.57	6.23
EW	5.80×10^{-2}	5.53×10^{-2}	5.32×10^{-2}
CR_{cor} (mm/y)	8.65×10^{-4}	7.39×10^{-4}	1.40×10^{-4}
Passivation region (mV)	>1100	>1100	200

4. Conclusion

- 1) The three HEAs prepared by SPS at 1150 °C are similar in microstructure and mainly consisting of Fe-rich FCC and Mo-rich FCC phases. With the increase of Si addition, the diffraction peak of Mo-rich FCC phase migrates to a higher angle, the lattice parameter of the phase decreases, and the intensity of the diffraction peak increases owing to the decrease of VEC and the increase of δ .
- 2) The hardness of HEAs increases with the enhancement of Si content, from 725 HV to 1186 HV. The wear resistance of FeCoCrNiMoSi_{0.5} is the best owing to the high proportion of abrasive wear. The wear resistance of FeCoCrNiMoSi_{1.0} and FeCoCrNiMoSi_{1.5} are inferior to that of FeCoCrNiMoSi_{0.5} because of the high proportion of delamination wear.
- 3) The three SPS FeCoCrNiMoSi_x show no phase change in the temperature range between 25 °C and 1150 °C, indicating strong high-temperature stability. FeCoCrNiMoSi_{0.5} presents the best anti-oxidation property.
- 4) The HEAs prepared by SPS show high corrosion resistance in 1 mol/L H₂SO₄ solution, while the increase of Si content could improve the corrosion resistance of the alloys. Among the three variants, FeCoCrNiMoSi_{1.5} HEA has the strongest corrosion resistance. However, the passive region of FeCoCrNiMoSi_{1.5} HEA is more narrow compared with those of FeCoCrNiMoSi_{0.5} and FeCoCrNiMoSi_{1.0} HEAs.

Credit authorship contribution statement

Yucheng Yang: Conceptualization, Data curation, Formal analysis, Investigation, Methodology, Writing - original draft. **Yaojia Ren:** Conceptualization, Methodology.

Yanwen Tian: Conceptualization. **Kaiyang Li:** Conceptualization, writing - review & editing. **Weidong Zhang:** Conceptualization, Methodology. **Quan Shan:**

Conceptualization, Methodology. **Yingtao Tian:** Conceptualization, Methodology g.

Qianli Huang: Conceptualization, Methodology. **Hong Wu:** Funding acquisition, Writing - review & editing.

Declaration of Competing Interest

The authors declared that they do not have any commercial or associative interest that represents conflicts of interest in connection with the work submitted.

Acknowledgements

This work was supported by the National Natural Science Foundation of China (Grant No. 52111530193) and Fundamental Research Funds for the Central University of Central South University (No. 2021ZZTS0098).

Reference

- [1] J.W. Yeh, S.-K. Chen, S.-J. Lin, J.-Y. Gan, T.-S. Chin, T.-T. Shun, C.-H. Tsau, S.-Y. Chang, Nanostructured High-Entropy Alloys with Multiple Principal Elements: Novel Alloy Design Concepts and Outcomes, *Advanced Engineering Materials* 6(5) 299-303.
- [2] T. Zhu, H. Wu, R. Zhou, N. Zhang, Y. Yin, L. Liang, Y. Liu, J. Li, Q. Shan, Q. Li, W. Huang, Microstructures and Tribological Properties of TiC Reinforced FeCoNiCuAl High-Entropy Alloy at Normal and Elevated Temperature, *Metals* 10(3) (2020).
- [3] A. Fu, W. Guo, B. Liu, Y. Cao, L. Xu, Q. Fang, H. Yang, Y. Liu, A particle reinforced NbTaTiV refractory high entropy alloy based composite with attractive mechanical properties, *Journal of Alloys And Compounds* 815 (2020).
- [4] C. Dai, T. Zhao, C. Du, Z. Liu, D. Zhang, Effect of molybdenum content on the microstructure and corrosion behavior of FeCoCrNiMox high-entropy alloys, *Journal of Materials Science & Technology* 46 (2020) 64-73.
- [5] W. Li, X. Long, S. Huang, Q. Fang, C. Jiang, Elevated fatigue crack growth resistance of Mo alloyed CoCrFeNi high entropy alloys, *Engineering Fracture Mechanics* 218 (2019) 106579-.
- [6] E.P. George, W.A. Curtin, C.C. Tasan, High entropy alloys: A focused review of mechanical properties and deformation mechanisms, *Acta Materialia* 188 (2020) 435-474.
- [7] Q. Zhao, J. Li, Q. Fang, H. Feng, Effect of Al solute concentration on mechanical properties of AlxFeCuCrNi high-entropy alloys: A first-principles study, *Physica B-Condensed Matter* 566 (2019) 30-37.
- [8] P. Sathiyamoorthi, H.S. Kim, High-entropy alloys with heterogeneous microstructure: Processing and mechanical properties, *Progress in Materials Science* (2020) 100709.
- [9] C. Han, Q. Fang, Y. Shi, S.B. Tor, C.K. Chua, K. Zhou, Recent Advances on High-Entropy Alloys for 3D Printing, *Advanced Materials* 32(26) (2020) 1903855.
- [10] Y. Yao, Z. Huang, P. Xie, S.D. Lacey, R.J. Jacob, H. Xie, F. Chen, A. Nie, T. Pu, M. Rehwoldt, Carbothermal shock synthesis of high-entropy-alloy nanoparticles, *Science* 359(6383) (2018) 1489-1494.
- [11] J. Li, Q.H. Fang, B. Liu, Y.W. Liu, Y. Liu, Atomic-scale analysis of nanoindentation behavior of high-entropy alloy, *Journal of Micromechanics and Molecular Physics* 01(01) (2016) 1650001.
- [12] Z. Tang, T. Yuan, C.-W. Tsai, J.-W. Yeh, C.D. Lundin, P.K. Liaw, Fatigue behavior of a wrought Al_{0.5}CoCrCuFeNi two-phase high-entropy alloy, *Acta Materialia* 99 (2015) 247-258.
- [13] N. Li, S. Wu, D. Ouyang, J. Zhang, L. Liu, Fe-based metallic glass reinforced FeCoCrNiMn high entropy alloy through selective laser melting, *Journal of Alloys and Compounds* 822 (2020) 153695.
- [14] H. Wu, L.X. Liang, X.D. Lan, Y. Yin, M. Song, R.D. Li, Y. Liu, H.O. Yang, L. Liu, A.H. Cai, Q.X. Li, W.D. Huang, Tribological and biological behaviors of laser clad Ti-based metallic glass composite coatings, *Applied Surface Science* 507 (2020).
- [15] T. Zhang, L. Xin, F. Wu, R. Zhao, J. Xiang, M. Chen, S. Jiang, Y. Huang, S. Chen, Microstructure and mechanical properties of Fe_xCoCrNiMn high-entropy alloys, *Journal of Materials Science & Technology* 35(10) (2019) 2331-2335.
- [16] B. Cai, B. Liu, S. Kabra, Y. Wang, K. Yan, P.D. Lee, Y. Liu, Deformation mechanisms of Mo alloyed FeCoCrNi high entropy alloy: In situ neutron diffraction, *Acta Materialia* 127 (2017) 471-480.

- [17] G.M. Poletaev, I.V. Zorya, M.D. Starostenkov, Role of point defects in self-diffusion along low-angle twist boundaries in fcc metals: A molecular dynamics study, *Journal of Micromechanics and Molecular Physics* 03(01n02) (2018) 1850001.
- [18] R. Sokkalingam, K. Sivaprasad, M. Duraiselvam, V. Muthupandi, K.G. Prashanth, Novel welding of Al_{0.5}CoCrFeNi high-entropy alloy: Corrosion behavior, *Journal of Alloys and Compounds* 817 (2020) 153163.
- [19] Y.J. Ren, L.X. Liang, Q. Shan, A.H. Cai, J.G. Du, Q.L. Huang, S.F. Liu, X. Yang, Y.T. Tian, H. Wu, Effect of volumetric energy density on microstructure and tribological properties of FeCoNiCuAl high-entropy alloy produced by laser powder bed fusion, *Virtual and Physical Prototyping* 15 (2020) 543-554.
- [20] R. Zhou, G. Chen, B. Liu, J. Wang, L. Han, Y. Liu, Microstructures and wear behaviour of (FeCoCrNi)_{1-x}(WC)_x high entropy alloy composites, *International Journal of Refractory Metals and Hard Materials* 75 (2018) 56-62.
- [21] P. Chauhan, S. Yebaji, V.N. Nadakuduru, T. Shanmugasundaram, Development of a novel light weight Al₃₅Cr₁₄Mg₆Ti₃V₁₀ high entropy alloy using mechanical alloying and spark plasma sintering, *Journal of Alloys and Compounds* 820 (2020) 153367.
- [22] S.P. Fitzgerald, Structure and dynamics of crowdion defects in bcc metals, *Journal of Micromechanics and Molecular Physics* 03(03-04) (2018) 1840003.
- [23] A. Fourmont, S. Le Gallet, O. Politano, C. Desgranges, F. Baras, Effects of planetary ball milling on AlCoCrFeNi high entropy alloys prepared by Spark Plasma Sintering: Experiments and molecular dynamics study, *Journal of Alloys and Compounds* 820 (2020) 153448.
- [24] A.I. Yurkova, V.V. Cherniavsky, V. Bolbut, M. Krüger, I. Bogomol, Structure formation and mechanical properties of the high-entropy AlCuNiFeCr alloy prepared by mechanical alloying and spark plasma sintering, *Journal of Alloys and Compounds* 786 (2019) 139-148.
- [25] Y. Hong, N. Zhang, L. Xiong, Nanoscale plastic deformation mechanisms of single crystalline silicon under compression, tension and indentation, *Journal of Micromechanics and Molecular Physics* 01(03n04) (2016) 1640007.
- [26] L.R. Kanyane, N. Malatji, A.P.I. Popoola, O.S.I. Fayomi, Synthesis of equi-atomic Ti-Al-Mo-Si-Ni high entropy alloy via spark plasma sintering technique: Evolution of microstructure, wear, corrosion and oxidation behaviour, *Results in Physics* 14 (2019).
- [27] M.-H. Tsai, J.-W. Yeh, J.-Y. Gan, Diffusion barrier properties of AlMoNbSiTaTiVZr high-entropy alloy layer between copper and silicon, *Thin Solid Films* 516(16) (2008) 5527-5530.
- [28] A. Kumar, P. Dhekne, A.K. Swarnakar, M.K. Chopkar, Analysis of Si addition on phase formation in AlCoCrCuFeNiSix high entropy alloys, *Materials Letters* 188 (2017) 73-76.
- [29] R. Babilas, W. Lonski, P. Borylo, M. Kadziolka-Gawel, P. Gebara, A. Radon, The influence of cooling rate, chromium and silicon addition on the structure and properties of AlCoCrFeNiSi high entropy alloys, *Journal of Magnetism and Magnetic Materials* 502 (2020) 166492.
- [30] B. Gorr, F. Mueller, H.J. Christ, T. Mueller, H. Chen, A. Kauffmann, M. Heilmaier, High temperature oxidation behavior of an equimolar refractory metal-based alloy 20Nb20Mo20Cr20Ti20Al with and without Si addition, *Journal of Alloys and Compounds* 688 (2016) 468-477.
- [31] J.H. Chen, P.N. Chen, P.H. Hua, M.C. Chen, Y.Y. Chang, W. Wu, Deposition of Multicomponent Alloys on Low-Carbon Steel Using Gas Tungsten Arc Welding (GTAW) Cladding Process, *Materials Transactions* 50(3) (2009) 689-694.
- [32] M. Zhang, T. Yuan, R. Li, Effect of spark plasma sintering on microstructure and friction characteristics of boron carbide, *Journal of Micromechanics and Molecular Physics* 03(01-02) (2017).

- [33] Alexander, L. Elbert, X-ray diffraction procedures for polycrystalline and amorphous materials, John Wiley & Sons, Inc1974.
- [34] X.L. Niu, L.J. Wang, D. Sun, J. Julius, Research on microstructure and electrochemical properties of $\text{Al}_x\text{FeCoCrNiCu}$ ($x=0.25, 0.5, 1.0$) high-entropy alloys, *Journal of Functional Materials* 44(4) (2013) 532-535.
- [35] S. Guo, L. Mei, The fractional variational iteration method using He's polynomials, *Physics Letters A* 375(3) (2011) 309-313.
- [36] Inoue, Akihisa, High Strength Bulk Amorphous Alloys with Low Critical Cooling Rates (Overview), *Materials Transactions Jim* 36(7) (2007) 866-875.
- [37] X. Yang, Y. Zhang, Prediction of high-entropy stabilized solid-solution in multi-component alloys, *Materials Chemistry and Physics* 132(2) (2012) 233-238.
- [38] J.F. Archard, Contact and Rubbing of Flat Surfaces, *Journal of Applied Physics* 24(8) (1953) 981-988.
- [39] J.H. Chen, P.N. Chen, C.M. Lin, C.M. Chang, Y.Y. Chang, W. Wu, Microstructure and wear properties of multicomponent alloy cladding formed by gas tungsten arc welding (GTAW), *Surface & Coatings Technology* 203(20) (2009) 3231-3234.
- [40] J.A. Badán, E. Navarrete-Astorga, R. Henríquez, F. Martín, R.E. Marotti, J.R. Ramos-Barrado, E.A. Dalchiele, Optical properties of silver nanoparticles deposited onto silicon substrates by different soft-solution processing techniques, *Optical Materials* 100 (2020) 109651.
- [41] W.H. Liu, Z.P. Lu, J.Y. He, J.H. Luan, Z.J. Wang, B. Liu, Y. Liu, M.W. Chen, C.T. Liu, Ductile CoCrFeNiMox high entropy alloys strengthened by hard intermetallic phases, *Acta Materialia* 116 (2016) 332-342.
- [42] Q. Wu, Z. Wang, F. He, J. Li, J. Wang, Revealing the Selection of σ and μ Phases in CoCrFeNiMox High Entropy Alloys by CALPHAD, *Journal of Phase Equilibria and Diffusion* 39(4) (2018) 446-453.
- [43] G. Deng, A.K. Tieu, L. Su, P. Wang, L. Wang, X. Lan, S. Cui, H. Zhu, Investigation into reciprocating dry sliding friction and wear properties of bulk CoCrFeNiMo high entropy alloys fabricated by spark plasma sintering and subsequent cold rolling processes: Role of Mo element concentration, *Wear* 460-461 (2020) 203440.
- [44] Y. Peng, W. Zhang, T. Li, M. Zhang, B. Liu, Y. Liu, L. Wang, S. Hu, Effect of WC content on microstructures and mechanical properties of FeCoCrNi high-entropy alloy/WC composite coatings by plasma cladding, *Surface & Coatings Technology* 385 (2020) 125326.
- [45] S. Xiao, K.A. Laux, H. Wang, F. Hu, H.-J. Sue, Physical correlation between abrasive wear performance and scratch resistance in model polyurethane elastomers, *Wear* 418 (2019) 281-289.
- [46] Stachowiak, W. Gwidon, Adhesion and Adhesive Wear, *Engineering Tribology* (2006) 553-572.
- [47] G.W. Stachowiak, A.W. Batchelor, Abrasive, Erosive and Cavitation Wear, *Engineering Tribology* (Third Edition) (2006) 501-551.
- [48] H. Wu, J. Ren, Q. Huang, X. Zai, L. Liu, C. Chen, S. Liu, X. Yang, R. Li, Effect of laser parameters on microstructure, metallurgical defects and property of AlSi10Mg printed by selective laser melting, *Journal of Micromechanics and Molecular Physics* 02(04) (2017) 1750017.
- [49] N.P. Suh, An overview of the delamination theory of wear, *Wear* 44(1) (1977) 1-16.
- [50] R. Aghababaei, On the origins of third-body particle formation during adhesive wear, *Wear* 426 (2019) 1076-1081.
- [51] L. Qiao, A. Bao, Y. Wang, Y. Liu, Z. Lai, J. Zhu, Thermophysical properties and high temperature oxidation behavior of FeCrNiAl0.5 multi-component alloys, *Intermetallics* 126 (2020).

- [52] S. Sheikh, M.K. Bijaksana, A. Motallebzadeh, S. Shafeie, A. Lozinko, L. Gan, T.-K. Tsao, U. Klement, D. Canadinc, H. Murakami, S. Guo, Accelerated oxidation in ductile refractory high-entropy alloys, *Intermetallics* 97 (2018) 58-66.
- [53] Y. Shinzato, Y. Saito, M. Yoshino, H. Yukawa, M. Morinaga, T. Baba, H. Nakai, Energy expression of the chemical bond between atoms in metal oxides, *Journal of Physics and Chemistry of Solids* 72(7) (2011) 853-861.
- [54] J.S. Dunning, D.E. Alman, J.C. Rawers, Influence of Silicon and Aluminum Additions on the Oxidation Resistance of a Lean-Chromium Stainless Steel, *Oxidation of Metals* 57(5-6) (2002) 409-425.
- [55] F. Mueller, B. Gorr, H.-J. Christ, H. Chen, A. Kauffmann, M. Heilmaier, Effect of microalloying with silicon on high temperature oxidation resistance of novel refractory high-entropy alloy Ta-Mo-Cr-Ti-Al, *Materials at High Temperatures* 35(1-3) (2018) 168-176.
- [56] Y. Xu, W. Li, L. Qu, X. Yang, B. Song, R. Lupoi, S. Yin, Solid-state cold spraying of FeCoCrNiMn high-entropy alloy: an insight into microstructure evolution and oxidation behavior at 700-900 °C, *Journal of Materials Science & Technology* 68 (2021) 172-183.
- [57] G. Laplanche, U.F. Volkert, G. Eggeler, E.P. George, Oxidation Behavior of the CrMnFeCoNi High-Entropy Alloy, *Oxidation of Metals* 85(5) (2016) 629-645.
- [58] W. Kai, C.C. Li, F.P. Cheng, K.P. Chu, R.T. Huang, L.W. Tsay, J.J. Kai, Air-oxidation of FeCoNiCr-based quinary high-entropy alloys at 700–900°C, *Corrosion Science* 121 (2017) 116-125.
- [59] D. Huang, J. Lu, Y. Zhuang, C. Tian, Y. Li, The role of Nb on the high temperature oxidation behavior of CoCrFeMnNb_xNi high-entropy alloys, *Corrosion Science* 158 (2019) 108088.
- [60] Standard practice for preparing, cleaning, and evaluating corrosion test specimens, *Astm* (2003).
- [61] O.D. Ofuyekpone, O.G. Utu, B.O. Onyekpe, Corrosion inhibition for alloy 304L (UNS S30403) in H₂SO₄ 1M solution by *Centrosema pubescens* leaves extract, *Applied Surface Science Advances* 3 (2021) 100061.
- [62] H. Liu, F. Huang, W. Yuan, Q. Hu, J. Liu, Y.F. Cheng, Essential role of element Si in corrosion resistance of a bridge steel in chloride atmosphere, *Corrosion Science* 173 (2020) 108758.
- [63] S.W. Dean, *Corrosion Testing of Materials with Metallic and Inorganic Coatings*, (1987) 177-192.
- [64] S.W. Dean, Jr., W. D. France, Jr., and S. J. Ketcham, Handbook on corrosion testing and evaluation, *Journal of The Electrochemical Society* 120(2) (1971) 173-174.
- [65] R. Baboian, *Electrochemical Techniques For Corrosion*, Electrochemical Techniques For Corrosion, Houston, TX, 1977.
- [66] E. Ura-Binczyk, N. Homazava, A. Ulrich, R. Hauert, M. Lewandowska, K.J. Kurzydowski, P. Schmutz, Passivation of Al–Cr–Fe and Al–Cu–Fe–Cr complex metallic alloys in 1M H₂SO₄ and 1M NaOH solutions, *Corrosion Science* 53(5) (2011) 1825-1837.
- [67] B. Normand, A. Pierre, J. Pagetti, Electrochemical and surface studies of the passive layers grown on sputter-deposited nitrogen-stainless steel alloys in 1M H₂SO₄ solution, *Corrosion Science* 37(10) (1995) 1537-1549.
- [68] M.M. Osman, R.A. El-Ghazawy, A.M. Al-Sabagh, Corrosion inhibitor of some surfactants derived from maleic-oleic acid adduct on mild steel in 1 M H₂SO₄, *Materials Chemistry and Physics* 80(1) (2003) 55-62.
- [69] H. Ashassi-Sorkhabi, Z. Ghasemi, D. Seifzadeh, The inhibition effect of some amino acids towards the corrosion of aluminum in 1M HCl+1M H₂SO₄ solution, *Applied Surface Science* 249(1) (2005) 408-418.

- [70] H.R. Zhou, W. Yao, C.W. Du, S.P. Song, R. Wu, Corrosion Behavior of the Al₂Cu Intermetallic Compound and Coupled Al₂Cu/Al, *International Journal of Electrochemical Science* 12(10) (2017) 9542-9554.
- [71] X.L. Shang, Z.J. Wang, F. He, J.C. Wang, J.J. Li, J.K. Yu, The intrinsic mechanism of corrosion resistance for FCC high entropy alloys, *Science China Technological Sciences* 61(2) (2018) 189-196.
- [72] B. Ren, R.-F. Zhao, Z.-X. Liu, S.-K. Guan, H.-S. Zhang, Microstructure and properties of Al_{0.3}CrFe_{1.5}MnNi_{0.5}Ti and Al_{0.3}CrFe_{1.5}MnNi_{0.5}Six high-entropy alloys, *Rare Metals* 33(2) (2014) 149-154.
- [73] S. Zheng, Z. Cai, J. Pu, C. Zeng, L. Wang, Passivation behavior of VAlTiCrSi amorphous high-entropy alloy film with a high corrosion-resistance in artificial sea water, *Applied Surface Science* 542 (2021) 148520.
- [74] T. Li, L. Liu, B. Zhang, Y. Li, F. Wang, An investigation on the continuous and uniform thin membrane passive film formed on sputtered nanocrystalline stainless steel, *Corrosion Science* 104 (2016) 71-83.
- [75] J. Oudar, Corrosion on the atomic scale, *British Corrosion Journal* 25(1) (1990) 21-29.